Check for updates

Cost-effective screen printing approach for Ce/Nd-doped ZnAl$_2$O$_4$ films: tuning crystallinity induced by the substrate†

Rocio E. Rojas-Hernandez, [ID] *[a] Fernando Rubio-Marcos, [ID] [b] Jallouli Necib,[a] Mati Danilson, [ID] [c] José F. Fernandez [ID] [b] and Irina Hussainova [ID] [a]

Near-infrared (NIR) emitting phosphors are currently receiving considerable attention owing to their high demand in various applications, such as light detection and ranging (LiDAR), short-range communications, security, biosensing and night vision lighting applications. The miniaturization of photonic components demands the integration of thin films into exploitable devices. In this context, NIR emitting ZnAl$_2$O$_4$:Ce/Nd films of hundreds of nanometer thickness are synthesized using a scalable and cost-efficient approach to screen printing. Cerium co-doping is responsible for the Nd emission in the NIR through energy transfer by exciting the films under UV excitation at around 360 nm. Through the proper design of ink, dense Nd/Ce doped ZnAl$_2$O$_4$ ceramic films were produced using polycrystalline alumina. The use of polycrystalline alumina substrates opens up new opportunities because this ceramic is a cheap and well-known substrate for optoelectronic packaging. During manufacturing, as a direct effect of predominant crystal growth over the polycrystalline alumina substrate, an increase in emission intensity is achieved. The results obtained by X-ray photoelectron (XPS) and X-ray absorption near edge spectroscopy (XANES) serve to determine the oxidation state of Ce. The findings of this study indicate that a higher concentration of Ce^{4+} promotes NIR emission. This study may contribute to a better understanding of film production processes of films based on the ZnAl$_2$O$_4$ matrix and guide future studies on films for NIR emitters.

Introduction

Near infrared (NIR) luminescent materials have emerged as promising candidates in many applications nowadays owing to their wide potential range in solar cells, photonic devices, light sources, opto-electronics and bio-imaging[1–5] To date, most NIR luminescent materials have been produced in the form of particles, ranging from micro to nano sizes. Recently, the number of research works on nanoscale materials has significantly increased because of their use as fluorescent probes for biological imaging. However, there is also a strong demand for NIR-emitting materials in the form of thin film.[6] NIR-emitting particles can be embedded into a matrix of synthesized films; however, this strategy usually implies a multi-step process and/

or encapsulation techniques in which the scattering phenomenon and non-homogeneity reduce the luminescence response. To solve the issues, magnetron sputtering, pulsed electron deposition, pulsed laser deposition and atomic layer deposition are used as the deposition techniques for producing luminescent films.[7–9] However, these strategies require expensive and complex systems. Recently, an intensive research effort has been directed towards the development of cost-efficient and high-performance printed films through direct approaches.

Using aerosol–jet printing and inkjet printing, relatively high accuracy can be achieved.[10] However, if high scalability is the goal, the films can be produced with cost-effective technology, such as screen printing,[11] which has already been employed in various fields, such as clothing, product labels, printed electronics, and solar cells,[12] to prepare continuous films or patterns.[13] Moreover, luminescence films can be deposited on both rigid and flexible substrates, opening up new application fields.[14,15] Usually, screen-printing is implemented to produce films of micrometer thickness; some studies have demonstrated the possibility of deposition of submicron films by tuning the printing pastes.[16] However, the study of an economical way to fabricate NIR luminescent films by screen printing is far from complete.

[a] Department of Mechanical and Industrial Engineering, Tallinn University of Technology, Ehitajate 5, 19180 Tallinn, Estonia. E-mail: rocio.rojas@taltech.ee
[b] Electroceramic Department, Instituto de Cerámica y Vidrio, CSIC, Kelsen 5, 28049, Madrid, Spain
[c] Department of Material and Environmental Technology, Tallinn University of Technology, Ehitajate 5, 19180 Tallinn, Estonia
† Electronic supplementary information (ESI) available. See DOI: https://doi.org/10.1039/d3cp02005c

This journal is © the Owner Societies 2023

Phys. Chem. Chem. Phys., 2023, **25**, 15829–15838 | **15829**

From a fundamental viewpoint, one of the possible effective NIR emitters in the form of films is luminescent materials based on aluminates, in particular zinc aluminate films doped with Nd and Ce. Moreover, efforts have recently focused on controlling the composition and growth of the spinel because of the formation of secondary phases. Zinc aluminate films are synthesized using a photochemical route by representing $ZnAl_2O_4$ as the main phase and ZnO as the secondary phase after annealing at 1100 °C.[17] Annealed at 1100 °C, green-emitting $ZnAl_2O_4$:Mn^{2+} phosphor thin films are deposited by a sol–gel spin coating route. The procedure allows film thickness modulation from 165 to 850 nm through the variation of the number of coating layers; the achieved emission intensity has demonstrated a strong dependency on the annealing temperature and film thickness.[18] Moreover, interconnected microstructural $ZnAl_2O_4$ films are also obtained by applying the sol–gel method, where the topography of $ZnAl_2O_4$ films can be varied by adjusting the heating rate.[19]

The formation of ZnO/$ZnAl_2O_4$ nanocomposite thin films is evaluated by Ultrasonic Spray Pyrolysis on Glass and Si(111) substrates, demonstrating that Zn/Al molar ratios affect the final composition through the formation of various polymorphs within the Zn_2SiO_4–ZnO–$ZnAl_2O_4$ system.[20] In addition, DC/RF magnetron sputtering technique is used to deposit $ZnAl_2O_4$ films by applying the power of 80 watts up to 140 watts (step size 20 watts) to the aluminum (Al) source and tuning the formation of $ZnAl_2O_4$.[21] The catalytic activity is revealed and attributed to the presence of the spinel $ZnAl_2O_4$ phase when the ALD deposition of ZnO on γ-Al_2O_3 is addressed.[22]

In this study, Ce and Nd are chosen as dopants to produce luminescent films based on zinc aluminate because Ce and Nd are considered promising candidates to promote emission by adding cerium. Specifically, as a potential sensitizer, cerium is incorporated into different hosts.[23] Other strategies, such as the introduction of alkali metal ions, can also considerably promote luminescence performance.[24] Our recent study demonstrates that the $ZnAl_2O_4$ is a suitable matrix for both dopants.[25] However, the host $ZnAl_2O_4$, which is known as a catalytic material, is transparent conductive oxide and sintering additive.[26–30] Visible emission is observed for the undoped material;[31–33] recently, deep-ultraviolet emission has been reported for Rare-Earth-Free $ZnAl_2O_4$ nanofibers,[34] which indicates the potential of this host matrix.

By employing a squeegee, a paste and a screen, a film is prepared on a flat substrate using the screen printing method. The formulation of the paste is crucial, together with the drying and annealing processes, to densify the film. The removal of organics during the drying process can result in a high porosity of the film, which hinders the necking and growth of the grains. The ink, also called a paste, mainly comprises 4 components: ceramic loading, solvent, binder and dispersant. The ratio between components affects the ink rheology and, consequently, the quality of the end product. Previously, we demonstrated the fabrication of films based on $SrAl_2O_4$:Eu^{2+},Dy^{3+} using a screen printing method assisted by a molten salt flux.[35] In this study, the eutectic molten salt mixture (NaCl–KCl) is employed to develop $ZnAl_2O_4$ submicrometer films over polycrystalline alumina. The densification, homogeneity and phase formation are enhanced by the molten salt added, which acts as a liquid phase boosting the rearrangement and dissolution of inorganic loading and the solubility of the substrate, which is exploited as a raw material to form the phase based on zinc aluminate. The molten salt volatilizes after the sintering process, accomplishing the objective of incorporation.

The aim of this study is threefold: (i) to optimize the ink formulation in the presence or absence of molten salt flux and to estimate different ratios of Zn in promoting the formation of the $ZnAl_2O_4$ phase; (ii) to elaborate a procedure for the deposition of inks onto polycrystalline alumina-based substrates, and (iii) to evaluate the effect of dopants (Ce and Nd) on the luminescence response of the film.

In our previous paper,[36] we demonstrated that luminescent (hk0)-textured $ZnAl_2O_4$:Nd,Ce sub-micron films over sapphire substrates can be successfully obtained. To further exploit the potential of the proposed screen-printing technique and obtain better properties using more versatile substrates, polycrystalline alumina substrates are employed. Considering that the proposed route should be applied to substrates with different reactivities, different ink formulations were detailed, and the effect of the Ce oxidation state on the luminescent response of the film has been thoroughly studied.

The results indicate that an adequate compositional engineering strategy plays a fundamental role in the fabrication of homogeneous $ZnAl_2O_4$-based films with high optical performance. Precise control of the phase crystallinity of the films is a mandatory requirement for obtaining a highly efficient end product.

Experimental section

Film preparation

$ZnAl_2O_4$ films were prepared using a screen printing technique assisted by a molten salt flux. Prior to deposition, ultrasonic cleaning of the substrate surface in ethanol (polycrystalline Al_2O_3, 10 × 25 × 1 mm) and substrate drying in a stream of air were carried out. The screen printing ink was prepared by mixing 60 wt% of the inorganic vehicle of precursors with particles from 1 μm to 7 μm and 40 wt% of the organic vehicle composed of α-terpineol solvent, 2-(2-butoxyethoxy) ethyl acetate plasticizer and DuPont™ 8250 thinner according to previously reported procedure.[35]

To homogenize the ink, both organic and inorganic components were loaded into 250 mL zirconia jars with zirconia balls and homogenized by a planetary ball milling (Model YKM-1). The milling process was performed at a rotation speed of 250 rpm for 8 hours. The chloride salt mixture composed of NaCl and KCl was homogenized before, including all the other inorganic components, such as ZnO (Symrise GmbH), CeO_2 (Evonik Degussa) and Nd_2O_3 (Metall Rare Earth Limited, 99.5%). The mol ratio of Nd was fixed to x = 0.02, and the Ce

15830 | *Phys. Chem. Chem. Phys.*, 2023, **25**, 15829–15838

This journal is © the Owner Societies 2023

was varied between $0.02 \leq x \leq 0.06$. Owing to the initial high viscosity of the ink, a suitable processing method is required to sufficiently disperse the agglomerates and aggregates into the primary particles. Therefore, three-roll milling was used for the dispersion, exploiting the internal shear and impact forces generated from the movement of the three rollers (employing a roller's gap of 15 μm and a rotation speed of 20 rpm) to break down agglomerates and aggregates.

Thereafter, the ink was deposited by screen-printing (DEK 65 screen-printing machine with a polyester 325 mesh) with a snap-off distance of 0.5 mm. The deposited ink layer was dried in an oven using a multi-step process at 150, 195, 270, 386 and 425 °C to remove the organic carrier, maintaining a slow heating rate of 0.5 °C min^{-1}. Subsequently, the thermal treatment was conducted at 1200 °C in the air for 2 h. This temperature was selected to ensure the complete removal of the eutectic salt used as flux according to the previous procedure developed by the authors.[37]

Structural and microstructural characterization

X-ray diffraction analysis was carried out using a Cu-Kα radiation source at 40 kV in ($\theta/2\theta$) Bragg–Brentano geometry (Rigaku SmartLab SE). Scanning electron microscopy (SEM) characterization was performed by employing an FE-SEM Zeiss ULTRA-55, Germany. The surfaces of the films and their profiles were analyzed to determine the thickness. A 3D optical profilometer Bruker ContourGT-K0+ was employed to determine the roughness of the alumina substrates and ZnAl$_2$O$_4$ films. Crystallite sizes were calculated using the Scherrer equation as follows:

$$D = \frac{K\lambda}{B\cos\theta} \tag{1}$$

where D is the crystallite size (nm), k is a constant, in our case 0.9, λ is the wavelength of the X-ray radiation, B is the full width at half maximum of the diffraction peak and θ is the Bragg's or diffraction angle.

X-ray absorption near-edge structure spectroscopy (XANES) measurements were performed at the ALBA synchrotron facility in the CLAESS beamline. The data collection of the Ce L$_3$-edge was done in fluorescence mode at room temperature, in which the signal was acquired with a 6-channel silicon drift detector (SDD) Xspress3 from a Quantum Detector. Multiple spectra were acquired for each film, and the average for each of them was obtained by employing the Athena software.[38] X-ray photoelectron spectroscopy (XPS) analysis was performed using a Kratos Analytical Axis Ultra DLD spectrometer. The device has the following monochromatic X-ray sources: Al Kα and an achromatic Mg Kα/Al Kα dual anode. The films were placed on a stainless-steel sample bar, and the XPS spectra were acquired at a take-off angle of 90° from the surface. Kratos Vision 2.2.10 software was employed to determine the relative atomic concentrations of the elements using Shirley background subtraction to calculate the relative atomic concentrations.

Optical characterization

Photoluminescence measurements in the visible range were carried out at room temperature using a Fluorolog-3, HORIBA Jobin Yvon system equipped with a xenon lamp, where the samples were excited at 359 and 740 nm. The excitation spectrum was acquired by fixing the emission at 1060 nm.

Results and discussion

Effect of zinc oxide content on ink formulation

To manufacture homogeneous ZnAl$_2$O$_4$-based films, it is necessary to understand the reaction mechanisms of raw materials with the substrate. To achieve this aim, three concentrations of ZnO in the ink were evaluated to ensure an adequate reaction to form the ZnAl$_2$O$_4$ phase. Fig. 1 displays the XRD patterns of films heat treated at 1200 °C, which were taken from three inks containing different amounts of zinc oxide, designated as 1Zn : 1Al, 0.5Zn : 1Al and 0.25Zn : 1Al. The PDF standard patterns of ZnO, ZnAl$_2$O$_4$ and Al$_2$O$_3$ provided by the Joint Committee on Powder Diffraction Standards (Powder Diffraction File (PDF)) corresponding to the cards PDF: 04-003-2106, PDF: 00-010-0173 and PDF: 01-074-1138 are shown in the bottom of Fig. 1. The XRD reflections are marked with a black circle symbol "○", red square symbol "□" and blue diamond symbol "◇", corresponding to the allowed Bragg reflections
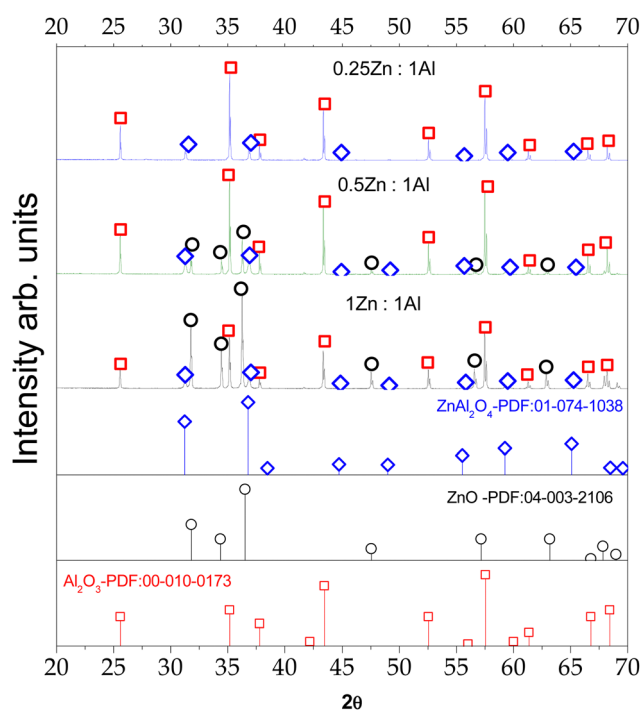

Fig. 1 Effect of zinc oxide content on the ink formulation: XRD of films synthesized at 1200 °C by including three contents of zinc oxide, such as 1Zn : 1Al, 0.5Zn : 1Al and 0.25Zn : 1Al. Red, blue and black symbols indicated the presence of diffraction peaks for Al$_2$O$_3$, ZnAl$_2$O$_4$ and ZnO, respectively. Each standard pattern of the raw materials, ZnO (PDF: 04-003-2106), the Al$_2$O$_3$ (PDF: 00-010-0173) and the ZnAl$_2$O$_4$ (PDF: 01-074-1138) are included below the XRD of the films.

This journal is © the Owner Societies 2023

Phys. Chem. Chem. Phys., 2023, **25**, 15829–15838 | **15831**

for ZnO, and Al_2O_3 and $ZnAl_2O_4$, respectively. It is noteworthy that the diffraction patterns are free from the components of the molten salt used, indicating the effective thermal removal of the flux. A rich formulation of zinc oxide (1Zn : 1Al) mainly yields the formation of ZnO with the insignificant formation of $ZnAl_2O_4$. ZnO is still present in the formulation with a reduced content of zinc oxide (0.5Zn : 1Al). Further reduction of ZnO (0.25Zn : 1Al) resulted in the development of only $ZnAl_2O_4$ as the main phase. For all three diffraction patterns presented, the contribution of the substrate is revealed. The experimental values of $ZnAl_2O_4$ unit-cell parameters for the films were calculated to be a = 8.0905 (25) Å and Vol = 528.89 Å^3, a = 8.0902 (13) Å and Vol = 529.59 Å^3 and a = 8.0902 (25) Å and Vol = 529.52 Å^3 for the films designated, such as 0.25Zn : 1Al, 0.5Zn : 1Al and 1Zn : 1Al, respectively. The lattice parameter a and the volume V were unaffected by the incorporation of excess ZnO. Therefore, a Zn : Al ratio of 0.25Zn : Al in the ink may be considered optimal, allowing the production of $ZnAl_2O_4$ as a single phase with cubic symmetry. To gain deeper insights into the extent of spinel inversion, we conducted Rietveld refinement, as depicted in Fig. S1 (ESI†). Through meticulous refinement of site occupation fractions, we determined a remarkably low spinel inversion degree of 0.082 for the $ZnAl_2O_4$ film synthesized with a Zn : Al ratio of 0.25. This finding attests to the exceptional crystalline structure of the film, which exhibits minimal perturbations in the occupation of crystallographic sites. The molten salt system provides a fast process for the dissolution–precipitation of Zn^{2+} cations. However, the diffusion of such cations through the Al_2O_3 crystal lattice is the kinetic limiting factor for the formation of the zinc aluminate structure. Thus, unreacted ZnO remains in films with ratios of 1Zn : 1Al and 0.5Zn : 1Al.

The relationships between microstructure and the Zn : Al ratio in the films were studied by FE-SEM, as shown in Fig. 2a–j. Fig. 2a and b presents low and high magnification SEM images of the surface-view microstructure of the polycrystalline alumina substrate. The substrate surface was polished to mean surface roughness (R_a) of 0.043 μm. SEM micrographs of film surfaces of different ZnO ratios are shown in Fig. 2c, d and g–i.

The top surfaces of the films with 1Zn : 1Al (Fig. 2c) and 0.5Zn : 1Al (Fig. 2d) ratios exhibit an inhomogeneous layer with small particles loosely arranged on the substrate. Two areas are distinguished in the top-surface view of both films, and areas marked with numbers 1 and 3 appear to be more homogeneous without unreacted particles on the top. However, the areas marked as 2 and 4 on panels c and d depicted in Fig. 2 mainly comprise particles that do not react with the substrate. From the EDS analysis (Fig. 2e and f) of both areas, it is confirmed that the EDS spectrum in the point of interest 1 and 3 detects Zn, Al and O related to $ZnAl_2O_4$ formation. However, the EDS spectra in points of interest 2 and 4 show mainly Zn and O; these results are correlated with the XRD, which confirmed the formation of ZnO. The top-surface and cross-section view of the film with the optimized ratio of ZnO (0.25Zn : 1Al) that yields the $ZnAl_2O_4$ film formation is shown in Fig. 2h–i. The higher magnification SEM micrograph shows a sufficient degree of recrystallization as the solubility limit is surpassed. When equilibrium is reached, the initial faceting of the surface is detected. Consequently, certain faceted shapes are visible on the surface. The surface roughness increases compared with the roughness of the alumina substrate to R_a = 0.13 μm. This value can represent a smooth surface considering that an unpolished alumina substrate has a mean roughness of 0.75–0.9 μm.[39] Surface texturing can likely be achieved by controlling
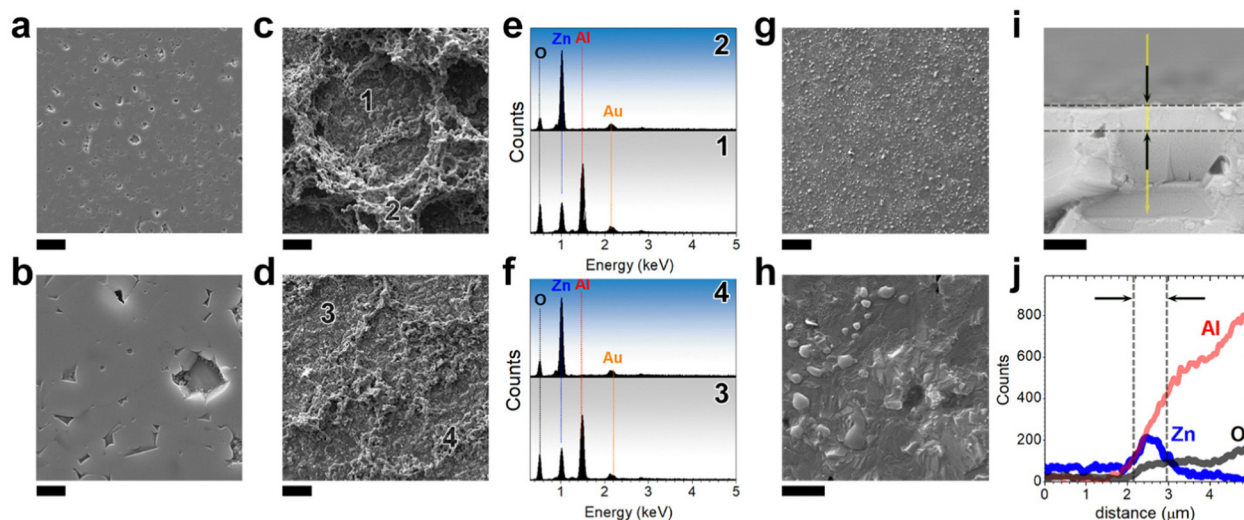
Fig. 2 Microstructure characterization of the films, including three contents of zinc oxide: (a and b) surface-view obtained by FE-SEM of the polycrystalline Al_2O_3 substrate polished. Scale bars, 10 μm and 2 μm, respectively. (c and d), FE-SEM images of the surface of the films deposited with various concentrations of ZnO, 1Zn : 1Al (panel c) and 0.5Zn : 1Al (panel d). Scale bars, 20 μm, respectively. (d–f) EDS analysis of the surface views in c and e. (g and h), FE-SEM images of the surface of the film deposited with a concentration of ZnO corresponding to 0.25Zn : 1Al. Scale bars, 20 μm and 1 μm, respectively. (i) Cross-sections of the film based on zinc aluminate obtained using the 0.25Zn : 1Al ink formulation. Scale bar: 1 micron. (j) EDS line-scan analysis of the cross-section in i.

15832 | *Phys. Chem. Chem. Phys.*, 2023, **25**, 15829–15838

This journal is © the Owner Societies 2023

crystallization and the diffusion–dissolution mechanism of $ZnAl_2O_4$ formation. The homogeneous and free of cracks surface is a consequence of both the optimized screen printing process and the molten salt-assisted reactive sintering. Adequate rheology of the ink is responsible for the production of the crack free green films under controlled drying up to 425 °C for the elimination of organic components. The SEM micrograph (Fig. 2i) of the cross-section depicts a uniform and dense thin film with ≈600 nm in thickness. The EDS line (Fig. 2j) scan profile detects zinc oxide at depths up to 600 nms from the surface; at a larger depth, the EDS detector distinguishes only Al and O related to the Al_2O_3 substrate. Thus, for the 0.25Zn : 1Al ratio, the proposed methodology results in homogeneous films with suitable control over the chemical composition, providing information about the formation of a $ZnAl_2O_4$ phase. The molten salt contributes to the reactive sintering mechanism by dissolving the Zn^{2+} cations and diffusing them into the alumina substrate. The surface tension of the eutectic liquid results in the development of a continuous film during melting that allows for the spinel reaction on all substrate surfaces. This process begins when the heating temperature exceeds the eutectic temperature of the molten salt. With an increase in the heating temperature, the components of the salt melt evaporate; at the selected temperature of 1200 °C, the flux is

removed, and reaction sintering is completed. The presence of ZnO in films with higher concentrations, such as 1Zn : 1Al and 0.5Zn : 1Al, indicates that there is a limited amount of Zn^{2+} cations diffusing into the alumina substrate owing to its crystal lattice packaging. It is worth mentioning here that, for the first time, dense $ZnAl_2O_4$ submicrometric films are obtained by applying the cost-efficient screen-printing process proposed in this study. Consequently, the optimized ratio of Zn : Al employed in the ink is fixed at 0.25Zn : 1Al for the rest of this study.

Development of $ZnAl_2O_4$ films doped and co-doped with Ce and Nd

To highlight the versatility of this technique, ink was added by the rare earths, Nd and Ce pair to understand the viability of their inclusion in the gahnite host. By engineering doping with Ce and Nd, the $ZnAl_2O_4$ matrix was modified to acquire a luminescence functional response. The phase composition and crystallinity of the films doped with Ce and Nd and annealed at 1200 °C for 2 hours in air were studied by XRD, and the diffractograms are shown in Fig. 3a. The formulations are designed by fixing the Nd content and co-doped with different Ce concentrations, such as $ZnAl_2O_4:xNd,yCe$ (x = 0.02, and y = 0.02, 0.04 and 0.06 mol ratio). The diffraction peaks confirm the
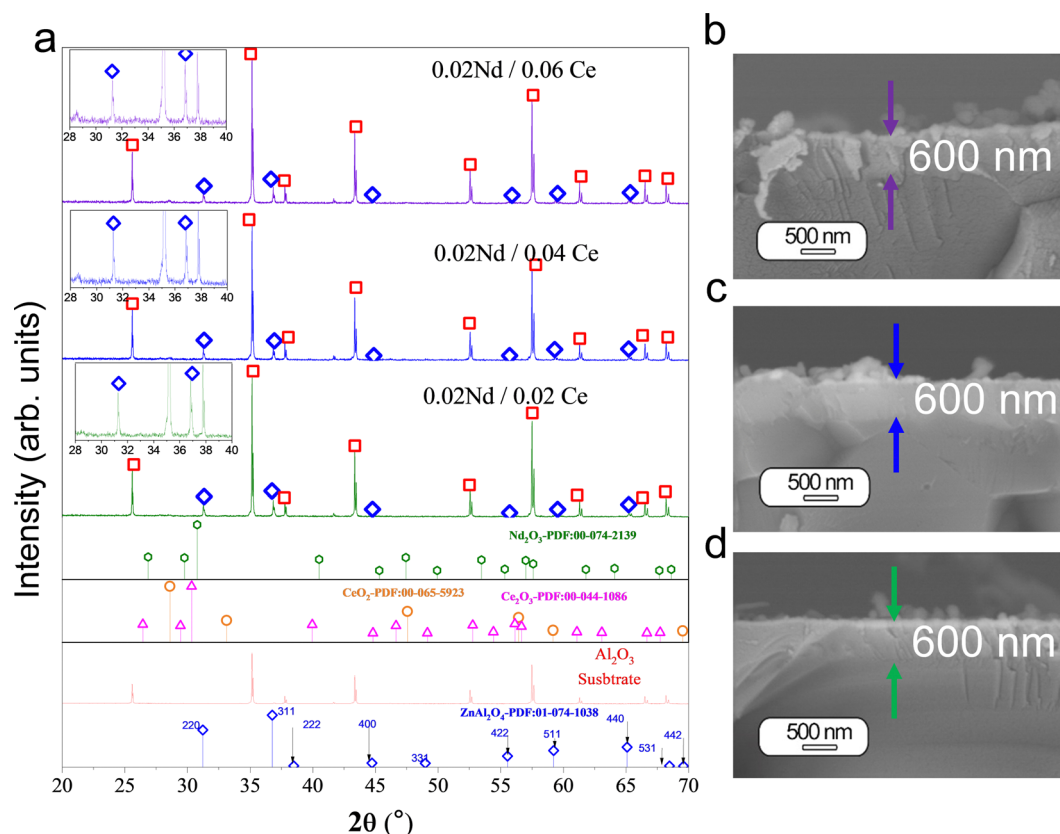
Fig. 3 $ZnAl_2O_4$ films doped and co-doped with Ce and Nd: (a) XRD of the films synthesized at 1200 °C by including a fixed content of Nd and three Ce concentrations: $ZnAl_2O_4:xNd,yCe$ (x = 0.02, and y = 0.02, 0.04 and 0.06 mol ratio). The XRD of the alumina substrate (red line) is shown at the bottom of figure a. The blue vertical marks at the bottom of the figure represent the reflection positions of zinc aluminates. (b–d) Cross-sectional views of the films synthesized in a.

polycrystalline nature of the $ZnAl_2O_4$ films. All peaks are in good agreement with the diffraction standard PDF: 01-074-1138. The inset illustrated in Fig. 3a reveals the two main diffraction reflections of the $ZnAl_2O_4$ cubic polymorph located at 31.29° and 36.86° 2θ, corresponding to planes (220) and (311), respectively. The contribution of the alumina substrate is detected and marked with the red square symbol "□". The crystallite size of the zinc aluminate films is 140 ± 7, 138 ± 7 and 136 ± 4 nm for the samples co-doped with 0.02Nd/0.02Ce, 0.02Nd/0.04Ce and 0.02Nd/0.06Ce, respectively. These crystallite sizes are large enough to provide enhanced luminescence properties because of the low grain boundary density.[40] The lattice parameter (a) and the volume of the unit cell (Vol) were calculated for the undoped film and the films co-doped with 0.02Nd/0.02Ce, 0.02Nd/0.04Ce and 0.02Nd/0.06Ce. The values obtained are a = 8.0905 (25) Å and Vol = 528.89 Å³, a = 8.0917 (12) Å and Vol = 529.51 Å³, a= 8.0926 (25) Å and Vol = 529.99 Å³ and a = 8.0928 (17) Å and Vol = 529.86 Å³ for the films undoped and co-doped with 0.02Nd/0.02Ce, 0.02Nd/0.04Ce and 0.02Nd/0.06Ce, respectively. The lattice parameter, a, and the volume of the unit cell, Vol, slightly increase as a function of Ce concentration, which indicates the effective doping of the structure. As shown in the cross-sectional SEM micrographs (Fig. 3b–d), the film thickness can be modulated to c.a. 600 nm for all co-doped formulations.

The viscosity (η) of the inks with different concentrations of dopants was measured in the shear rate range between 1 and 2000 s⁻¹ (ESI†, S2). The flow curves show that all inks exhibit a shear thinning behavior. The degree of shear thinning is quite similar for all inks. Therefore, it is expected that the viscosity will decrease for the effective transfer of the ink onto the substrate surface. During the screen printing process, viscosity changes as a function of the shear rate and time. Usually, a shear rate value around 1000 s⁻¹ is adopted when the ink penetrates the opened screen mesh.[41] The viscosity at a low shear rate serves only as a reference if there is any change in the ink properties. However, the measured viscosity as a function of the shear rate is almost similar for all inks prepared, demonstrating the reproducibility of the paste formulation and fabrication process, including homogenization and dispersion steps.

In summary, the absence of secondary phases in the doped films is a remarkable result, suggesting that the $ZnAl_2O_4$ matrix and both dopants form a suitable and stable solid solution. It is important to note that optimization of the ink formulation leads to the formation of $ZnAl_2O_4$ without secondary phases. The cross-sectional SEM images show homogeneous and dense films without cracks, which is a significant achievement because ceramic materials are usually difficult to sinter into crack-free films. Using our approach, the mismatch between the sintering shrinkage of the film and the substrate is minimized. The knowledge acquired in this study is useful for designing inks that can be applied to other systems based on aluminates.

Luminescence properties of the $ZnAl_2O_4$ films co-doped with Ce and Nd and their structural correlations

There are different ways to modulate the emission in a material. In this study, the enhancement of the NIR emission of $ZnAl_2O_4$ films by energy transfer from Ce to Nd is considered. It is known that the direct excitation of Nd in the UV is hindered owing to the low absorption cross-section in this wavelength range. Therefore, three cerium concentrations were studied; the films were excited under 357 nm excitation at RT, as shown in Fig. 4a. The films doped only with Nd and doped only with Ce were compared with the co-doped samples. In all samples, three emissions are observed and are characteristics of Nd^{3+}. The emission peaks positioned at 850 to 950 nm correspond to the $^4F_{3/2} \rightarrow {}^4I_{9/2}$ transition. The main emission located at 1000 to 1175 nm is assigned to the $^4F_{3/2} \rightarrow {}^4I_{11/2}$ transition, and other emissions appear at 1300 to 1400 nm corresponding to the $^4F_{3/2} \rightarrow {}^4I_{13/2}$ transition. To add the proof for energy transfer from Ce to Nd, the Nd single-doped materials are also excited by 357nm as a reference. It can be observed that the emission of Nd is almost not observable, as might be expected. The emission spectra under 740 nm are presented in Fig. 4b, and the excitation spectra b fixing the emission at 1060nm is demonstrated in Fig. 4c. Under 740 nm excitation, there is the presence of an emission band located at 1060 nm assigned to the direct excitation of Nd. The emission intensity under 740 nm excitation varies insignificantly as a function of the Ce concentration. This result is expected because Nd is excited directly and not through the cerium co-dopant. Nd^{3+} cation can also be excited by various wavelengths, as shown in the excitation spectra. In particular, the most intense band is located at 740 nm in the near infrared range. The intensity of the excitation band located at 357 nm slightly increases with Ce concentration from 0.02 to 0.06. However, for the material only doped with Nd, this excitation band is not present, indicating that the excitation band located at 357 nm is attributed to Ce. Here, the co-dopant allows for the absorption of excitation light in the UV, enhancing NIR emission. It has already been demonstrated that Ce co-dopant can enhance the NIR emission in the $ZnAl_2O_4$[25] system, as well as in other matrices, such as yttrium aluminium garnet (YAG), $Y_3Al_5O_{12}$ doped with Nd and Ce,[42,43] K_2CeO_3[44] and Li_2CeO_3.[45] Thus, we can identify that efficient energy transfer from Ce to Nd exists in this system. The schematic energy levels with transition, which may be involved in the energy transfer process, are demonstrated in Fig. S3 (see ESI†). Nd^{3+} has several energy levels, and some of them are in the UV region, having good overlap with Ce absorption. Thus, there are several channels for energy transfer from Ce to Nd. ^2P_j levels of Nd might be populated by energy transfer from Ce and Nd can then relax to a $^4F_{3/2}$ state by emitting phonons in several steps. Consequently, the NIR emission is obtained by transitions from $^4F_{3/2}$ to lower lying ^4I_j levels. Another possibility is that from 5D states, Nd can de-excite to $^4F_{3/2}$ level by cross relaxation, taking a nearby Nd cation to the excited state. However, further analyses are needed to establish the exact mechanism. However, the excitation band at 740 nm remains unchanged, as expected, because the Nd concentration is fixed at 002.

However, there is still an open question related to the presence of Ce^{3+} and Ce^{4+} ions and their role in the enhancement of NIR emission. Only a few studies have discussed the

15834 | *Phys. Chem. Chem. Phys.*, 2023, **25**, 15829–15838

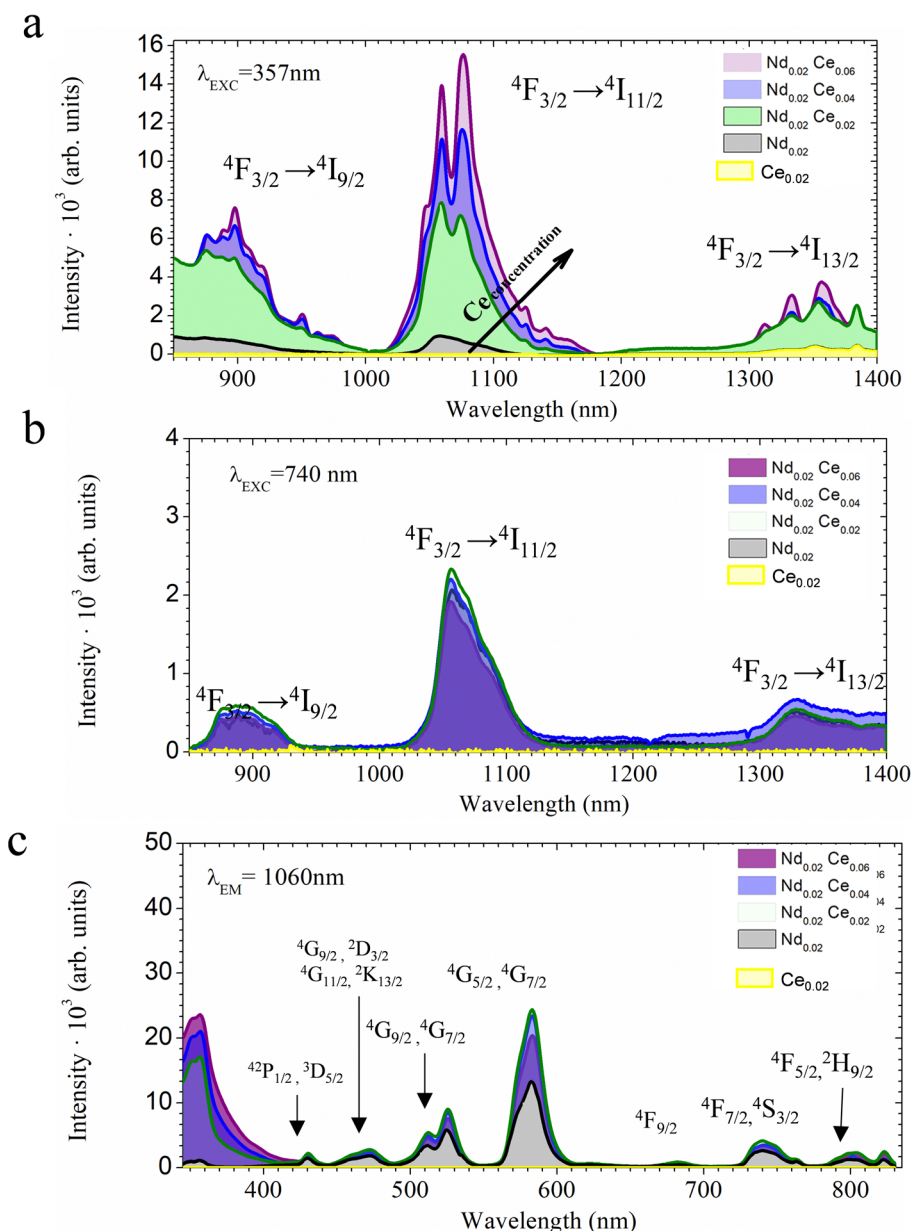This journal is © the Owner Societies 2023

Fig. 4 Luminescence characterization of the $ZnAl_2O_4$ films doped and co-doped with Ce and Nd: (a) emission spectra under 357 nm at RT of the films synthesized at 1200 °C by including a fixed content of Nd and three Ce concentrations, $ZnAl_2O_4$:xNd,yCe (x = 0.02, and y = 0.02, 0.04 and 0.06 mol ratio), the film only doped with Nd and the film doped with a concentration of Ce0.02. (b) Emission spectra under 740 nm. (c) Excitation spectra fixing the emission at 1060 nm.

presence of trivalent and tetravalent cerium in the luminescence process of Ce doped scintillators.[46] Bearing in mind assumptions that Ce^{4+} has an absorption band wider than Ce^{3+},[47] a higher absorption due to the charge transfer band of Ce^{4+} is expected. To establish the oxidation state of the films, XANES at Ce L_3-edge (5723 eV)[48] and XPS experiments were carried out. The normalized XANES spectra of the $ZnAl_2O_4$:xNd, yCe (x = 0.02, and y = 0.02, 0.04 and 0.06 mol ratio) samples with the reference spectra of CeO_2 and $Ce(NO_3)_3$ $6H_2O$ are shown in Fig. 5a. The CeO_2 and $Ce(NO_3)_3$ $6H_2O$ standards were used to perform the linear combination fitting (LC) to determine the Ce^{3+} and Ce^{4+} ratio.[25] $Ce(NO_3)_3$ $6H_2O$ reference shows

a sharp edge feature, while CeO_2 and $ZnAl_2O_4$ films doped with different Ce concentrations display a doublet.[49] The incorporation of higher concentrations of Ce up to 0.06 mol ratio comes with the stabilization of Ce^{4+} and turns into a higher intensity for the emission bands located at 1069 and 1077 nm, as shown in Fig. 5b. To further determine the oxidation state on the surface, XPS was acquired. Both trivalent Ce^{3+} and tetravalent Ce^{4+} are detected (Fig. 5c). The XPS spectra for the films are composed of two multiples attributed to $3d_{3/2}$ core holes and $3d_{5/2}$ spin-orbit split. Six of the peaks corresponding to final sates of Ce^{4+} and four to Ce^{3+} are detected. The six peaks located at 915.45, 905.45, 899.9, 897.3, 887, and 881.4 eV belong
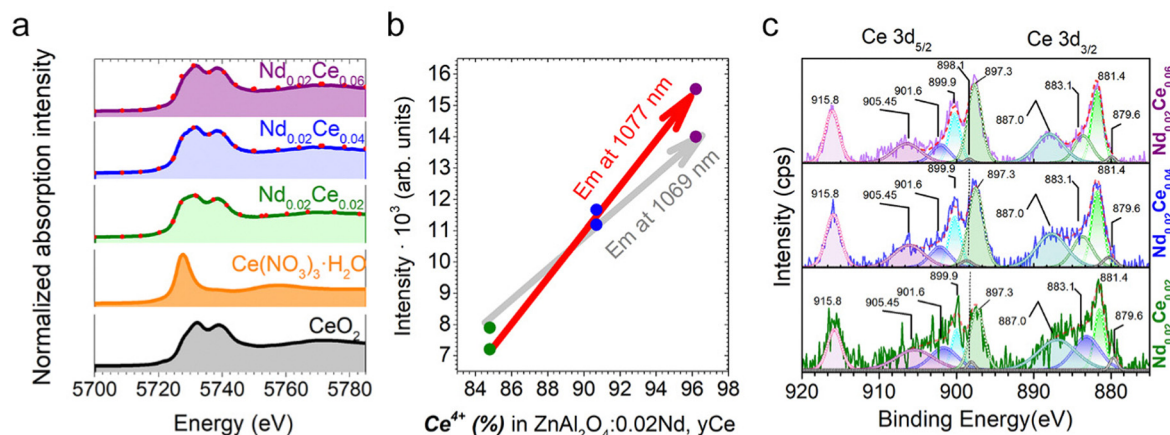
This journal is © the Owner Societies 2023

Phys. Chem. Chem. Phys., 2023, 25, 15829–15838 | 15835

Fig. 5 Structural characterization by XANES at Ce L_3-edge and XPS of the $ZnAl_2O_4$ films doped and co-doped with Ce and Nd: (a) XANES at Ce L_3-edge of the films synthesized with 0.02 Nd mol ratio and concentration of Ce from 0.02 to 0.06 mol ratio. At the bottom, the XANES of two references of cerium, cerium oxide and cerium nitrate are presented. The linear combination fitting is included in figure a by adding the dotted red line. Panel b shows the emission intensity of the peaks at 1069 and 1077 nm as a function of the Ce^{4+} calculated from the XANES at the Ce L_3-edge results. (c). The experimental solid line and fitted curves (dot curves for each peak and solid red line for the sum of the deconvolution) of the high-resolution XPS spectra of the Ce $3d_{3/2,5/2}$ lines.

to the Ce(IV) states; the peak located at 915.45 eV is the fingerprint of Ce^{4+}. The distinct line shapes located at 901.6, 898.1, 883.1 and 879.8 eV are assigned to Ce^{3+} states. All of the emission peaks are in good agreement with previous studies.[50,51]

Therefore, doping engineering with the Ce and Nd of $ZnAl_2O_4$ films leads to the stabilization of Ce^{4+}, promoting NIR emission. Moreover, increased Ce content enhances NIR emission, leading to a gradual increase in the presence of Ce^{4+}, which is associated with local structural homogeneity.

Conclusions

To expand the scope of the screen printing technique applied to the synthesis of NIR-emitting submicron films, herein, poly-crystalline alumina is used for the growth of the $ZnAl_2O_4$ spinel material. The ink formulation and scalable fabrication procedures were thoroughly evaluated. We revealed a molten salt-driven growth mechanism and designed a growth strategy, thus achieving crystallites with an average size of 140 nm, much larger than in previous reports. These crystallite sizes are large enough to enhance luminescence properties owing to a low grain boundary density. The substrate precursor *in situ* partici-pates in the reaction; by employing the eutectic molten salt mixture (NaCl–KCl), which promotes the surface reaction, con-trollable nucleation is achieved. Based on the XANES and XPS results, the cerium in the films exhibits a predominant tetra-valent state. Our proposed method improves the emission centered at 1069 and 1077 nm by applying high concentrations of cerium and by doping engineering with Ce and Nd. An adequate compositional engineering strategy plays a funda-mental role in the production of homogeneous films based on $ZnAl_2O_4$ with high optical performance. Our findings offer novel insights into controllable synthesis for thin films based on $ZnAl_2O_4$ and pave the way for the development of efficient

NIR emitters based on aluminate systems in next-generation functional devices.

Conflicts of interest

There are no conflicts of interest to declare.

References

1 C. T. Jackson, S. Jeong, G. F. Dorlhiac and M. P. Landry, Advances in engineering near-infrared luminescent materi-als, *iScience*, 2021, **24**, 102156.

2 F. Zhang and B. Z. Tang, Near-infrared luminescent probes for bioimaging and biosensing, *Chem. Sci.*, 2021, **12**, 3377–3378.

15836 | *Phys. Chem. Chem. Phys.*, 2023, **25**, 15829–15838

This journal is © the Owner Societies 2023

3 Y. Zhao, G. A. Meek, B. G. Levine and R. R. Lunt, Near-infrared harvesting transparent luminescent solar concentrators, *Adv. Opt. Mater.*, 2014, **2**, 606–611.

4 H. Yang, J. Xiahou, Q. Zhu and J. Li, Considerable improved near-infrared luminescence in ionic-free doped $ZnAl_2O_4$ by oxygen defects engineering, *J. Lumin.*, 2023, **253**, 119455.

5 M. Bungla, S. Chowdhari, M. Shanu, P. Pragya, V. Perumal, G. V. Prakash and A. K. Ganguli, $NaBiF_4:Yb^{3+},Tm^{3+}$ submicron particles as luminescent probes for in vitro imaging of cells, *Phys. Chem. Chem. Phys.*, 2023, **25**, 6131–6141.

6 A. E. Giba, P. Pigeat, S. Bruyere, H. Rinnert, F. Mücklich, R. Gago and D. Horwat, Ultraviolet optical excitation of near infrared emission of Yb-doped crystalline aluminum oxynitride thin films, *J. Appl. Phys.*, 2018, **124**(3), 033102.

7 E. Salas-colera, M. Tard, E. Garc, M. L. Crespillo, J. E. Muñoz-santiuste and B. Galiana, Development of Luminescent Nd-Doped LaNbO Compound Thin Film Growth by Magnetron Sputtering for the Improvement of Solar Cells, *Crystals*, 2023, **13**, 159.

8 S. Normani, G. Louvet, E. Baudet, M. Bouška, J. Gutwirth, F. Starecki, J. L. Doualan, Y. Ledemi, Y. Messaddeq, J. L. Adam, P. Němec and V. Nazabal, Comparative study of Er^{3+}-doped Ga–Ge–Sb–S thin films fabricated by sputtering and pulsed laser deposition, *Sci. Rep.*, 2020, **10**, 1–13.

9 M. N. Getz, O. Nilsen and P. A. Hansen, Sensors for optical thermometry based on luminescence from layered $YVO_4:Ln^{3+}$ (Ln = Nd, Sm, Eu, Dy, Ho, Er, Tm, Yb) thin films made by atomic layer deposition, *Sci. Rep.*, 2019, **9**, 1–11.

10 H. Minemawari, T. Yamada, H. Matsui, J. Y. Tsutsumi, S. Haas, R. Chiba, R. Kumai and T. Hasegawa, Inkjet printing of single-crystal films, *Nature*, 2011, **475**, 364–367.

11 X. Cao, H. Chen, X. Gu, B. Liu, W. Wang, Y. Cao, F. Wu and C. Zhou, Screen printing as a scalable and low-cost approach for rigid and flexible thin-film transistors using separated carbon nanotubes, *ACS Nano*, 2014, **8**, 12769–12776.

12 H. P. Kuo, H. A. Tsai, A. N. Huang and W. C. Pan, CIGS absorber preparation by non-vacuum particle-based screen printing and RTA densification, *Appl. Energy*, 2016, **164**, 1003–1011.

13 M. Gajadhur and P. Chmura, Lighting time analysis of water-based flexographic inks containing phosphorescent pigments, *Appl. Mater. Today*, 2023, **30**, 101719.

14 W. Yao, Q. Tian, J. Liu, Z. Wu, S. Cui, J. Ding, Z. Dai and W. Wu, Large-scale synthesis and screen printing of upconversion hexagonal-phase $NaYF_4:Yb^{3+},Tm^{3+}/Er^{3+}/Eu^{3+}$ plates for security applications, *J. Mater. Chem. C*, 2016, **4**, 6327–6335.

15 Y. Chen, T. Ke, S. Chen, X. He, M. Zhang, D. Li, J. Deng and Q. Zeng, Optical properties of flexible fluorescent films prepared by screen printing technology, *AIP Adv.*, 2018, **8**(5), 055008.

16 Z. Wan, M. Xu, Z. Fu, D. Li, A. Mei, Y. Hu, Y. Rong and H. Han, Screen printing process control for coating high throughput titanium dioxide films toward printable mesoscopic perovskite solar cells, *Front. Optoelectron.*, 2019, **12**, 344–351.

17 G. Cabello, L. Lillo, C. Caro, M. Seguel, C. Sandoval, G. E. Buono-Core, B. Chornik and M. Flores, A photochemical proposal for the preparation of $ZnAl_2O_4$ and $MgAl_2O_4$ thin films from β-diketonate complex precursors, *Mater. Res. Bull.*, 2016, **77**, 212–220.

18 I. B. Huang, Y. S. Chang, H. L. Chen, C. C. Hwang, C. J. Jian, Y. S. Chen and M. T. Tsai, Preparation and luminescence of green-emitting $ZnAl_2O_4:Mn^{2+}$ phosphor thin films, *Thin Solid Films*, 2014, **570**, 451–456.

19 Y. Wu, J. Du, K. L. Choy, L. L. Hench and J. Guo, Formation of interconnected microstructural $ZnAl_2O_4$ films prepared by sol–gel method, *Thin Solid Films*, 2005, **472**, 150–156.

20 S. Iaiche, C. Boukaous, D. Alamarguy, A. Djelloul and D. Hamana, Effect of solution concentration on ZnO/$ZnAl_2O_4$ nanocomposite thin films formation deposited by ultrasonic spray pyrolysis on glass and Si(111) substrates, *J. Nano Res.*, 2020, **63**, 10–30.

21 A. Jilani, I. S. Yahia, M. S. Abdel-wahab, A. A. Al-ghamdi and H. Alhummiany, Novel Control of the Synthesis and Band Gap of Zinc Aluminate ($ZnAl_2O_4$) by Using a DC/RF Sputtering Technique, *Silicon*, 2019, **11**, 577.

22 M. Nadjafi, A. M. Kierzkowska, A. Armutlulu, R. Verel, A. Fedorov, P. M. Abdala and C. R. Müller, Correlating the Structural Evolution of ZnO/Al_2O_3 to Spinel Zinc Aluminate with its Catalytic Performance in Propane Dehydrogenation, *J. Phys. Chem. C*, 2021, **125**, 14065–14074.

23 Z. Xia and R. Liu, Tunable Blue-Green Color Emission and Energy Transfer of, *J. Phys. Chem. C*, 2012, **116**, 15604–15609.

24 Y. Hu, X. Yan, L. Zhou, P. Chen, Q. Pang and Y. Chen, Improved Energy Transfer in Mn-Doped $Cs_3Cu_2I_5$ Microcrystals Induced by Localized Lattice Distortion, *J. Phys. Chem. Lett.*, 2022, **13**, 10786–10792.

25 R. E. Rojas-Hernandez, F. Rubio-Marcos, G. Gorni, C. Marini, M. Danilson, L. Pascual, R. U. Ichikawa, I. Hussainova and J. F. Fernandez, Enhancing NIR emission in $ZnAl_2O_4:Nd,Ce$ nanofibers by co-doping with Ce and Nd: A promising biomarker material with low cytotoxicity, *J. Mater. Chem. C*, 2021, **9**, 657–670.

26 D. P. Dutta, R. Ghildiyal and A. K. Tyagi, Luminescent properties of doped zinc aluminate and zinc gallate white light emitting nanophosphors prepared via sonochemical method, *J. Phys. Chem. C*, 2009, **113**, 16954–16961.

27 L. Cornu, M. Duttine, M. Gaudon and V. Jubera, Luminescence switch of Mn-Doped ZnAl2O4 powder with temperature, *J. Mater. Chem. C*, 2014, **2**, 9512–9522.

28 M. E. Foley, R. W. Meulenberg, J. R. McBride and G. F. Strouse, Eu^{3+}-Doped ZnB_2O_4 (B = Al^{3+}, Ga^{3+}) Nanospinels: An Efficient Red Phosphor, *Chem. Mater.*, 2015, **27**, 8362–8374.

29 N. Basavaraju, K. R. Priolkar, D. Gourier, S. K. Sharma, A. Bessière and B. Viana, The importance of inversion disorder in the visible light induced persistent luminescence in Cr^{3+} doped AB_2O_4 (A = Zn or Mg and B = Ga or Al), *Phys. Chem. Chem. Phys.*, 2015, **17**, 1790–1799.

30 Y. Zhang, R. Huang, H. Li, D. Hou, Z. Lin, J. Song, Y. Guo, H. Lin, C. Song, Z. Lin and J. Robertson, Germanium

This journal is © the Owner Societies 2023

Phys. Chem. Chem. Phys., 2023, **25**, 15829–15838 | **15837**

Paper

PCCP

substitution endowing Cr 3p-doped zinc aluminate phosphors with bright and super-long near-infrared persistent luminescence, *Acta Mater.*, 2018, **155**, 214–221.

31 A. A. Da Silva, A. S. Gonçalves, M. R. Davolosv and S. H. Santagneli, Al^{3+} environments in nanostructured $ZnAl_2O_4$ and their effects on the luminescence properties, *J. Nanosci. Nanotechnol.*, 2008, **8**, 5690–5695.

32 L. Cornu, M. Gaudon and V. Jubera, $ZnAl_2O_4$ as a potential sensor: Variation of luminescence with thermal history, *J. Mater. Chem. C*, 2013, **1**, 5419–5428.

33 N. Pathak, P. S. Ghosh, S. Saxena, D. Dutta, A. K. Yadav, D. Bhattacharyya, S. N. Jha and R. M. Kadam, Exploring defect-induced emission in $ZnAl_2O_4$: an exceptional color-Tunable phosphor material with diverse lifetimes, *Inorg. Chem.*, 2018, **57**, 3963–3982.

34 R. Rojas-Hernandez, F. Rubio-Marcos, I. Romet, A. Campo, G. Gorni, I. Hussainova, J. F. Fernandez and V. Nagirnyi, Deep-Ultraviolet Emitter: Rare-Earth-Free $ZnAl_2O_4$ Nanofibers via a Simple Wet Chemical Route, *Inorg. Chem.*, 2022, **61**, 11886–11896.

35 R. E. Rojas-hernandez, F. Rubio-marcos, A. Serrano, I. Hussainova and J. Francisco, Boosting phosphorescence e ffi ciency by crystal anisotropy in $SrAl_2O_4$:Eu,Dy textured ceramic layers, *J. Eur. Ceram. Soc.*, 2019, 0–1.

36 R. E. Rojas-Hernandez, F. Rubio-Marcos, A. Serrano, S. Román-Sánchez, J. F. Fernandez and I. Hussainova, Highly textured zinc aluminate: Nd, Ce films over sapphire for NIR emitting applications, *Ceram. Int.*, 2023, **49**(8), 13125–13130.

37 R. E. Rojas-Hernandez, F. Rubio-Marcos, R. H. Gonçalves, M. Á. Rodriguez, E. Véron, M. Allix, C. Bessada and J. F. Fernandez, Original Synthetic Route To Obtain a $SrAl_2O_4$ Phosphor by the Molten Salt Method: Insights into the Reaction Mechanism and Enhancement of the Persistent Luminescence, *Inorg. Chem.*, 2015, **54**, 9896–9907.

38 B. Ravel and M. Newville, *J. Synchrotron Radiat.*, 2005, **12**, 537–541.

39 Z. Qi, L. Liao, R. yue Wang, Y. gang Zhang and Z. fu Yuan, Roughness-dependent wetting and surface tension of molten lead on alumina, *Trans. Nonferrous Met. Soc. China*, 2021, **31**, 2511–2521.

40 R. E. Rojas-Hernandez, F. Rubio-Marcos, A. Serrano, A. Del and J. F. Fernandez, Precise Tuning of the Nanostructured

Surface leading to the Luminescence Enhancement in $SrAl_2O_4$ Based Core/Shell Structure, *Sci. Rep.*, 2017, **7**, 1–9.

41 M. Neidert, W. Zhang, D. Zhang and A. Kipka, Screen-printing simulation study on solar cell front side AG paste, *Conf. Rec. IEEE Photovoltaic Spec. Conf.*, 2008, 14–17.

42 P. Samuel, T. Yanagitani, H. Yagi, H. Nakao, K. I. Ueda and S. M. Babu, Efficient energy transfer between Ce^{3+} and Nd^{3+} in cerium codoped Nd: YAG laser quality transparent ceramics, *J. Alloys Compd.*, 2010, **507**, 475–478.

43 M. Yamaga, Y. Oda, H. Uno, K. Hasegawa, H. Ito and S. Mizuno, Energy transfer from Ce to Nd in $Y_3Al_5O_{12}$ ceramics, *Phys. Status Solidi C*, 2012, **9**, 2300–2303.

44 A. Vyas, C. P. Joshi and S. V. Moharil, Sensitization of nir emission by tetravalent cerium in K_2CeO_3:Nd,Yb, *J. Alloys Compd.*, 2018, **763**, 159–163.

45 P. K. Tawalare, V. B. Bhatkar, S. K. Omanwar and S. V. Moharil, Broad Band excited NIR emission in Li_2CeO_3:Nd/Yb phosphor for modification of solar spectrum, *J. Alloys Compd.*, 2019, **771**, 534–540.

46 D. Zhu, M. Nikl, W. Chewpraditkul and J. Li, Development and prospects of garnet ceramic scintillators: a review, *J. Adv. Ceram.*, 2022, **11**, 1825–1848.

47 C. K. Jørgensen, Electron Transfer Spectra, *Absorpt. Spectra Chem. Bond. Complexes*, 1962, **12**, 146–172.

48 V. Khanin, I. Venevtsev, K. Chernenko, V. Pankratov, K. Klementiev, T. van Swieten, A. J. van Bunningen, I. Vrubel, R. Shendrik, C. Ronda, P. Rodnyi and A. Meijerink, Exciton interaction with Ce^{3+} and Ce^{4+} ions in $(LuGd)_3(Ga,Al)_5O_{12}$ ceramics, *J. Lumin.*, 2021, **237**, 118150.

49 G. S. Henderson, F. M. F. De Groot and B. J. A. Moulton, *X-ray Absorption Near-Edge Structure (XANES) Spectroscopy*, 2014, **78**, 75–138.

50 E. Bêche, P. Charvin, D. Perarnau, S. Abanades and G. Flamant, Ce 3d XPS investigation of cerium oxides and mixed cerium oxide ($Ce_xTi_yO_z$), *Surf. Interface Anal.*, 2008, **40**, 264–267.

51 K. I. Maslakov, Y. A. Teterin, A. J. Popel, A. Y. Teterin, K. E. Ivanov, S. N. Kalmykov, V. G. Petrov, P. K. Petrov and I. Farnan, XPS study of ion irradiated and unirradiated CeO_2 bulk and thin film samples, *Appl. Surf. Sci.*, 2018, **448**, 154–162.

15838 | *Phys. Chem. Chem. Phys.*, 2023, **25**, 15829–15838

This journal is © the Owner Societies 2023